Inorganic Chemistry

Article

pubs.acs.org/IC

Red-Green Emitting and Superparamagnetic Nanomarkers Containing Fe_3O_4 Functionalized with Calixarene and Rare Earth Complexes

Latif U. Khan,[†] Hermi F. Brito,*[,†] Jorma Hölsä,[†,‡,§] Kleber R. Pirota,[∥] Diego Muraca,[∥] Maria C.F.C. Felinto,[⊥] Ercules E.S. Teotonio,[#] and Oscar L. Malta[∇]

[†]Institute of Chemistry, Department of Fundamental Chemistry, University of São Paulo, Av. Prof. Lineu Prestes, 748, 05508-000 São Paulo-SP, Brazil

[‡]Department of Chemistry and [§]Centre for Materials and Surfaces (MatSurf), University of Turku, FI-20014 Turku, Finland

[∥]Institute of Physics "Gleb Wataghin", Condensed Matter Physics Department, State University of Campinas (UNICAMP), 13083-859 Campinas-SP, Brazil

[⊥]Nuclear and Energy Research Institute (IPEN-CQMA), Av. Prof. Lineu Prestes, 2242, 05508-000 São Paulo-SP, Brazil

[#]Department of Chemistry, Federal University of Paraiba, 58051-970 João Pessoa-PB, Brazil

[∇]Department of Fundamental Chemistry, Federal University of Pernambuco, 50670-901, Recife-PE, Brazil

Supporting Information

ABSTRACT: The design of bifunctional magnetic luminescent nanomaterials containing Fe_3O_4 functionalized with rare earth ion complexes of calixarene and β-diketonate ligands is reported. Their preparation is accessible through a facile one-pot method. These novel Fe_3O_4@calix-Eu(TTA) (TTA = thenoyltrifluoroacetonate) and Fe_3O_4@calix-Tb(ACAC) (ACAC = acetylacetonate) magnetic luminescent nanomaterials show interesting superparamagnetic and photonic properties. The magnetic properties (M-H and ZFC/FC measurements) at temperatures of 5 and 300 K were explored to investigate the extent of coating and the crystallinity effect on the saturation magnetization values and blocking temperatures. Even though magnetite is a strong luminescence quencher, the coating of the Fe_3O_4 nanoparticles with synthetically functionalized rare earth complexes has overcome this difficulty. The intramolecular energy transfer from the T_1 excited triplet states of TTA and ACAC ligands to the emitting levels of Eu^{3+} and Tb^{3+} in the nanomaterials and emission efficiencies are presented and discussed, as well as the structural conclusions from the values of the 4f–4f intensity parameters in the case of the Eu^{3+} ion. These novel nanomaterials may act as the emitting layer for the red and green light for magnetic light-converting molecular devices (MLCMDs).

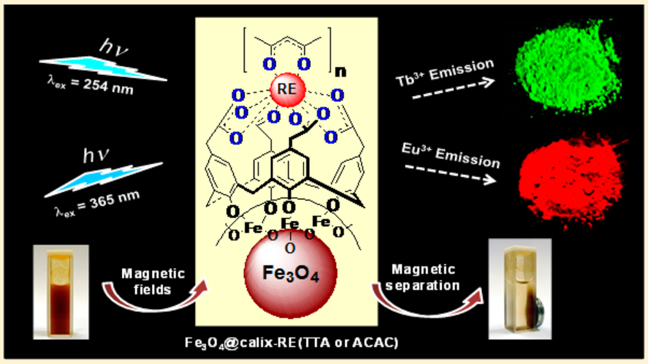

1. INTRODUCTION

In nature, smart materials that exhibit efficient optical and magnetic properties are very remarkable. For many applications in biotechnology, medicine, and quality inspection, this type of bifunctional material is sought for.[1] Nanomaterials with unique magnetic and photonic properties have also great potential in biological applications such as MRI contrast agents, drug delivery carriers, and biomarkers.[2−5] Several reports have focused on the synthesis and characterization of multifunctional nanomaterials, such as hybrid[6−8] as well as magnetic and optical core–shell ones.[9−13]

Magnetite nanoparticles have been the subject of extensive research in the past decades, owing to their remarkable applications:[14] great importance to biomineralization in natural resources, such as human brain,[15] carbonaceous chondrites,[16] magnetite production by microorganisms,[17−19] and as a magnetoreceptor in rainbow trout[20] and honeybees.[21] Magnetite can be also used as a significant tool for reduction of carbon dioxide and water. Cation excess Fe_3O_4 reduces carbon dioxide completely to carbon and reduces water to gaseous hydrogen.[22] In addition, magnetic oxide nanoparticles can be functionalized with carboxylates,[23,24] amines, or diols,[25] as well as with phosphates, phosphonates, and sulfonates,[26] to ensure the colloidal stability of these nanomaterials in an organic or aqueous medium. Ethylenediaminetetraacetic acid-functionalized Fe_3O_4 nanoparticles can be used for selective uptake of rare earths from aqueous solution.[27] Remarkably stable magnetite ferrofluids have been reported by utilizing for first time the *p*-sulfonato-calix[6 and 8]arenes and sulfonated *p*-

Received: August 7, 2014
Published: December 5, 2014

dx.doi.org/10.1021/ic5018856 | *Inorg. Chem.* 2014, 53, 12902−12910

benzylcalix[4,5,6, and 8]arenes as surfactants to coat the superparamagnetic magnetite nanoparticles.[28]

Calixarenes are macrocyclic molecules made up of *p*-substituted phenolic units linked by methylene bridges *ortho* to the hydroxyl groups. They are useful building blocks for hollow molecular scaffolds with easily functionalizable hydrophilic and hydrophobic lower and upper rims, respectively.[29] In supramolecular chemistry calixarenes are used for a variety of functions such as inclusion complexes,[30] molecular scaffolds,[31] and molecular recognition for rare earth ions (RE^{3+}).[32−34]

The growing interest in the luminescent materials containing RE^{3+} ions and their photonic applications is presently extended from laser physics to materials science, agriculture, and medical diagnostics.[35] Selected examples are phosphors for lighting and displays, lasers, optical telecommunications, security inks, anticounterfeiting tags, probes for luminescent immunoassays, and bioconjugates for photodynamic treatment of cancer.[36] Of great interest are the rare earth-based persistent luminescence[37] and polymer materials.[38]

The 4f energy levels are only slightly affected by the chemical environment due to the effective shielding of the 4f electrons by the filled 5s and 5p orbitals. Therefore, the absorption and emission spectra of the 4f intraconfigurational transitions of the RE^{3+} ions retain more or less their atomic character and similarities irrespective of the host matrix.

The luminescence properties of the RE^{3+} β-diketonate complexes[39,40] indicate that the organic ligands can act as good sensitizers (*antenna effect*) for the RE^{3+} ions. Therefore, the promising optical properties of several RE^{3+} ions have added a new field of research to the coordination chemistry. Among the luminescent materials studied, Eu^{3+} and Tb^{3+} complexes appear to be the most attractive ones because of their highly efficient red and green emissions, respectively, in the visible range featuring long emission lifetimes.

Aiming to optimize the emission quantum efficiency of the luminescent material, the ligand should be chosen according to the efficiency of the following processes: (a) absorption from the ground singlet to the excited singlet state of the ligand ($S_0 \rightarrow S_1$), (b) nonradiative decay to the triplet state via the intersystem crossing, and (c) nonradiative intramolecular energy transfer from the T_1 state of the ligand to the excited states of the RE^{3+} ion, $T_1(L) \rightarrow {}^{2S+1}L_J$ (RE^{3+}).[39]

In the present work, the one-pot syntheses as well as optical and magnetic properties are reported for two novel luminescent magnetic nanoparticles, namely, Fe_3O_4@calix-Eu(TTA) and Fe_3O_4@calix-Tb(ACAC), where TTA = thenoyltrifluoroacetonate and ACAC = acetylacetonate (Figure 1). On the basis of the magnetic properties at different temperatures, a superparamagnetic model considering magnetic interactions was used to better understand the magnetic behavior. From the technological point of view, the results obtained are very promising and show progress on the physical knowledge of superparamagnetic systems with dipolar interactions. Although magnetite is usually a strong luminescence quencher,[13] this difficulty was overcome by functionalizing the Fe_3O_4 nanoparticles with macrocyclic building block with in situ coprecipitation. The influence of the chemical structure of the ligand, magnetite, and organic moiety on the photoluminescence properties of the Eu^{3+} and Tb^{3+} ions was also studied to produce highly luminescent nanomaterials. The experimental intensity parameters (Ω_2 and Ω_4) and the radiative and nonradiative rates (A_{rad} and A_{nrad}) for the Eu^{3+} nanophosphor were calculated. The emission spectral features, the experimental emission quantum efficiency, and the emission lifetimes for these nanomaterials are also discussed.

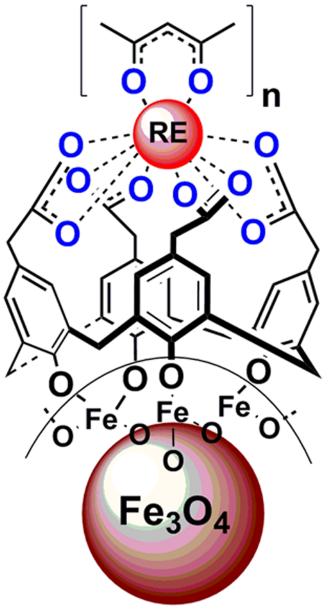

Figure 1. Schematic illustration of the structure of the magnetic and luminescent nanoparticles containing Fe_3O_4 functionalized with RE^{3+} complex of β-diketonate and calixarene as ligands (Fe_3O_4@calix-RE(TTA or ACAC)).

2. EXPERIMENTAL SECTION

2.1. Materials Preparation. *2.1.1. Magnetite Nanoparticles.* These were synthesized with coprecipitation under continuous flow of N_2. In this synthesis, a mixture of $FeCl_2·4H_2O$ and $FeCl_3·6H_2O$ in a 1:2 molar ratio was dissolved in ultrapure Milli-Q water under constant magnetic stirring,[28] followed by a dropwise addition of an aqueous NaOH solution (1.0 mol L^{-1}) until a stable black magnetite suspension was formed at pH ≈ 11. The aqueous suspension was stirred further at room temperature maintaining the N_2 flow for 2 h; thereafter, the Fe_3O_4 suspension was centrifuged, and the solid material was collected. After that, the black nanopowders were redispersed in ultrapure Milli-Q water and centrifuged again. This process was repeated three times to remove the base, and then the magnetite nanoparticles were dried in a vacuum desiccator.

2.1.2. Fe_3O_4@calix-Eu(TTA). These bifunctional magnetic and red-emitting nanoparticles were prepared with a new one-pot method. The aqueous solution of 2.25 mmol of $FeCl_3·6H_2O$ and 1.15 mmol of $FeCl_2·4H_2O$ in 100 mL of ultrapure Milli-Q water was stirred under a N_2 flow. Then, 0.27 g (0.41 mmol) of *p*-tetrakiscarboxymethylcalix-4-arene macrocycle (calix) was slowly added to the reaction mixture. A NaOH solution (18 mL, 1.0 mol L^{-1}) was added dropwise until a stable brown-colored magnetite suspension was formed maintaining the pH at 11. After the solution was stirred for 3 h at room temperature, the pH was adjusted to 7 with a dropwise addition of dilute aqueous HCl (1.0 mol L^{-1}). A solution of 0.36 g (1.64 mmol) of thenoyltrifluoroacetone (HTTA) in ethanol was added slowly to the reaction mixture. Then, an aqueous solution of 1.64 mmol of $EuCl_3·6H_2O$ in ultrapure Milli-Q water was added dropwise along with adjustment of pH to 7 by dropwise addition of the NaOH solution. The reaction mixture was stirred at room temperature for 60 h under N_2. The solid Fe_3O_4 material was separated from the aqueous suspension by centrifugation and decantation of the supernatant with applied external magnet. The collected solid material was washed five times with Milli-Q water and chloroform and dried in a vacuum desiccator to get the brown-colored Fe_3O_4@calix-Eu(TTA) nanomaterials.

Scheme 1. Preparation of Magnetic and Luminescent Fe_3O_4@calix-Eu(TTA) and Fe_3O_4@calix-Tb(ACAC) Nanomaterials through One-Pot Method, Using Fe_3O_4@calix and RE^{3+} Complexes

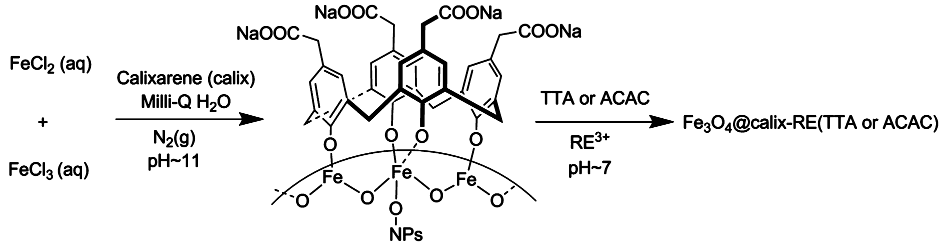

2.1.3. *Fe_3O_4@calix-Tb(ACAC).* The bifunctional magnetic and green-emitting nanoparticles were prepared by the same procedure as described for the Eu^{3+} system (Section 2.1.2), which also led to a brown powder. In this synthesis, 0.5 mmol of $FeCl_3{\cdot}6H_2O$ and 0.25 mmol of $FeCl_2{\cdot}4H_2O$ were mixed in 30 mL of ultrapure Milli-Q water, and 0.06 g (0.091 mmol) of *p*-tetrakiscarboxymethylcalix-4-arene macrocycle was added. Following the procedure, 6-fold excess of acetylacetone (HACAC) and 4-fold excess of $TbCl_3{\cdot}6H_2O$ were utilized to get the Fe_3O_4@calix-Tb(ACAC) nanomaterial.

2.2. Characterization. The elemental analysis of carbon and hydrogen of the macrocyclic sample was carried out using a PerkinElmer 2400 CHN Elemental Analyzer. The NMR spectra of the calixarene macrocycle were recorded by Varian Gemini 200 MHz Fourier Transform (FT) Nuclear Magnetic Resonance equipment. The X-ray Powder Diffraction (XPD) data were recorded by a Rigaku Miniflex II diffractometer using Cu $K_{\alpha 1}$ radiation (λ = 1.5406 Å) in the 2θ range of 10 to 80°. The Fourier transform infrared (FTIR) absorption spectra were measured using KBr pellet technique with a Bomem MB100 FTIR from 400 to 4000 cm^{-1}.

Transmission electron microscopy (TEM) images and electron diffraction were measured with a JEOL JEM 2100 LaB_6 TEM, acceleration voltage: 200 kV. The sample particles were dispersed in Milli-Q water and sonicated for 15 min. Samples were prepared by drying the water-dispersed nanoparticles on a carbon-coated copper grid, and images were acquired with the sample on a single-tilt sample holder and a Gatan ES500W TV camera. Small-angle X-ray scattering (SAXS) experiments were recorded at the Centro Nacional de Pesquisa em Energia e Materiais (CNPEM), Brazilian Synchrotron Light Laboratory (LNLS), using the beamline SAXS 2 in the energy range from 6.0 to 11.0 keV. The samples were prepared as colloidal solutions in Milli-Q water (v/v 5%).

Direct-current magnetic properties were studied using a Quantum Design MPMS XL SQUID magnetometer. Zero field cooling/field cooling (ZFC/FC) measurements were done to characterize the static magnetic properties of the nanomaterials. The measurements were carried out as follows: the sample was first cooled from 300 to 5 K in a zero magnetic field, then a static magnetic field of 50 Oe was applied, and the magnetization was measured increasing the temperature to room temperature (300 K). Subsequently, the samples were cooled to 5 K under the same applied magnetic field (50 Oe), and the magnetization was measured while warming the samples from 5 to 300 K. The magnetization as a function of the applied field between −2 and +2 T was measured at selected temperatures from 5 to 300 K.

The excitation and emission spectra of the Eu^{3+} and Tb^{3+} nanomaterials were recorded with a SPEX FL212 Fluorolog-2 spectrofluorometer using a 450 W xenon lamp as an excitation source and two 0.22 m double grating SPEX 1680 monochromators for dispersing the radiation. Luminescence decay of the Eu^{3+} nanomaterial was measured using the SPEX 1934D phosphorimeter accessory attached to the 150 W pulsed xenon lamp. The entire luminescence setup was fully controlled by a DM3000F spectroscopic computer program, and the spectral intensities were automatically corrected for the photomultiplier (PMT) response.

3. RESULTS AND DISCUSSION

The calixarene macrocycle was synthesized by a synthetic protocol, involving five steps of reactions (see Supporting Information, Scheme S1), with overall yield of 55%, as reported in the literature.[41−43] The whole synthetic route involves a crucial step of the Mannich reaction (Scheme S1, step 2), which was carried out by using aqueous dimethylamine (v/v 25−30%) and aqueous formaldehyde (v/v 37%) in the presence of glacial acetic acid. The yield of the corresponding reaction was raised from 15 to 99% by using 12-fold excess of aqueous dimethylamine (v/v 25−30%) and 12-fold excess of aqueous formaldehyde (v/v 37%); the reaction time was increased from 24 to 60 h as well. The yield of the Mannich reaction is favored by an increase in the concentration of reagents and time of reaction.

The structure of the calixarene macrocycle (calix) (Scheme S1, step 5) was confirmed by using spectroscopic techniques (FTIR, ^1H NMR, and ^{13}C NMR) and CHN elemental analysis. The FTIR spectrum of the calixarene macrocycle is dominated by a broad absorption band centered at 3180 cm^{-1}, which corresponds to the ν_{O-H} stretching of the phenolic unit of calixarene (see Supporting Information, Figure S2). The strong absorption band observed at 1705 cm^{-1} was assigned to the $\nu_{C=O}$ stretching of the carboxylic group. The absorption bands observed in the region of 1405−1480 cm^{-1} correspond to the $\nu_{C=C}$ stretching in the aromatic ring of the calixarene macrocycle. The ^1H NMR spectrum recorded at room temperature (200 MHz, deuterated dimethyl sulfoxide) closely matched the actual structure of the macrocycle, showing a resonance peak at δ 6.95 for the 8Ar−H of the calixarene (calix-H) (see Supporting Information, Figure S3). In addition, the broad singlet resonance peak at δ 3.82 corresponds to 8H of methylene ($ArCH_2Ar$). The resonance peak at δ 3.27 represents the 8H of methylene (CH_2COO) in the macrocycle. The ^1H NMR spectrum also shows one additional peak for water molecules at δ 3.42.

The elemental analysis of CHN found (%): C: 61.75, H: 5.38 was very close to the calculated ones: C: 60.84, H: 5.39. These results indicate that the calixarene macrocycle has three accommodated water molecules (Scheme S1, step 5). The spectroscopic and elemental analyses were carried out after drying the macrocycle (**5**) with a vacuum dryer at 95 °C for 5 h. It is suggested that the hydrophobic cavity of the calixarene moiety contains water molecules when the hydrophobic guest is absent.[44] All of the found spectroscopic data (FTIR, ^1H NMR, and ^{13}C NMR) were in agreement with those reported in the literature[43] (see Supporting Information, Figure S3).

The whole synthetic pathway of the novel bifunctional magnetic and optical nanoparticles Fe_3O_4@calix-Eu(TTA) and Fe_3O_4@calix-Tb(ACAC) is dominated by two steps of reactions (Scheme 1). The one-pot method was designed for the entire synthesis, and the magnetic luminescent nanoparticles were then successfully prepared. According to the literature,[28,45] the Fe_3O_4 nanoparticles are stabilized by *p*-sulfonato-calixarenes and sulfonated *p*-benzylcalix arenes. On the basis of studies, the assumed schematic structure of the Fe_3O_4@calix-Eu(TTA) and Fe_3O_4@calix-Tb(ACAC) nanomaterials, as shown in Figure 1, is consistent with the previous results.

3.1. Structural and Morphological Characterization of Fe_3O_4@calix-Eu(TTA) and Fe_3O_4@calix-Tb(ACAC) Nanomaterials. As shown in the XPD pattern (Figure 2) of magnetite, the diffraction reflections can be indexed as the face-centered cubic (fcc) lattice of the Fe_3O_4 phase (XPD reference pattern of Fe_3O_4, ICDD/PDF 19−629). After coating the magnetite (Fe_3O_4) with the calixarene macrocycle and RE^{3+} complexes, in addition to the Fe_3O_4 reflections, the diffraction patterns of the magnetic luminescent nanoparticles also show mainly characteristic reflections of an amorphous phase.

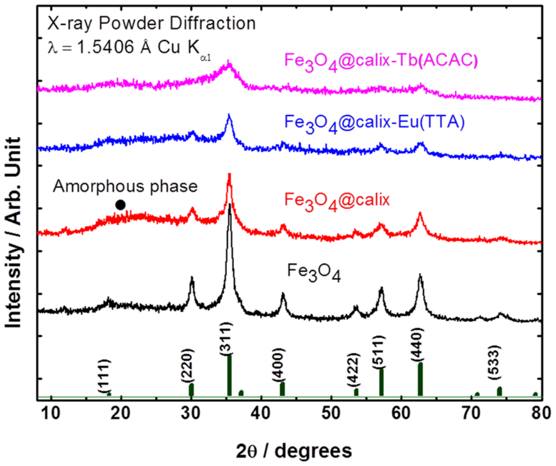

Figure 2. X-ray powder diffraction patterns of Fe_3O_4, calixarene macrocycle (calix) coated magnetite nanoparticles (Fe_3O_4@calix), Fe_3O_4@calix-Eu(TTA), and Fe_3O_4@calix-Tb(ACAC) nanomaterials.

The FTIR absorption spectra of the Fe_3O_4@calix-Eu(TTA) and Fe_3O_4@calix-Tb(ACAC) nanomaterials show the broad absorption bands centered at 3500 cm^{-1}, indicating the presence of the water molecules in the nanomaterials (see Supporting Information, Figure S4). The strong absorption band observed for the free ligand at 1705 cm^{-1} corresponds to the $\nu_{C=O}$ stretching of carboxylic group of the calixarene macrocycle. It was red-shifted in the spectra of all the nanomaterials and appeared in the spectral range from 1450 to 1670 cm^{-1}. This result suggests that the carboxylic group of the macrocycle is coordinated to the RE^{3+} ions. Moreover, the absorption bands in the region of 1395−1560 cm^{-1} correspond to the $\nu_{C=C}$ stretching in the aromatic ring of the calixarene macrocycle. Similarly, the spectra of these nanomaterials show additional absorption bands at 1602 and 1612 cm^{-1} due to the C═O stretching vibrations of ACAC and TTA ligands, respectively. This result gives support to the carbonyl moiety of both *β*-diketonate ligands coordinating to the RE^{3+} ions.

The high-resolution TEM (HRTEM) images and small-angle X-ray scattering (SAXS) analyses show that the Fe_3O_4@calix-Eu(TTA) and Fe_3O_4@calix-Tb(ACAC) nanoparticles are probably separated from each other and nonaggregated when compared to the magnetite nanoparticles (Figure 3). This is probably due to the coating of magnetite nanocrystals with a

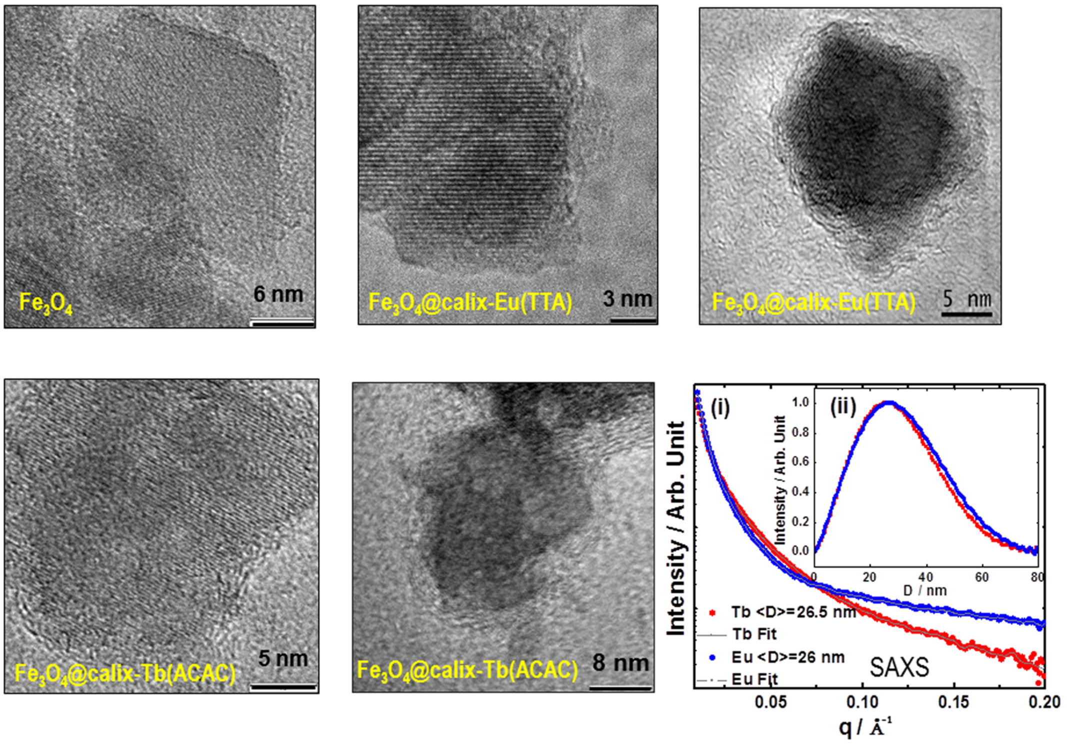

Figure 3. High-resolution TEM images of (clockwise from top left): Fe_3O_4, Fe_3O_4@calix-Eu(TTA) nanoparticles (different magnifications), Fe_3O_4@calix-Tb(ACAC) one (different magnifications). SAXS profile of Fe_3O_4@calix-Eu(TTA) and Fe_3O_4@calix-Tb(ACAC) shows (i) scattering intensity as a function of the scattering vector and (ii) the size distributions obtained from the fit on SAXS data for the Fe_3O_4@calix-Eu(TTA) and Fe_3O_4@calix-Tb(ACAC).

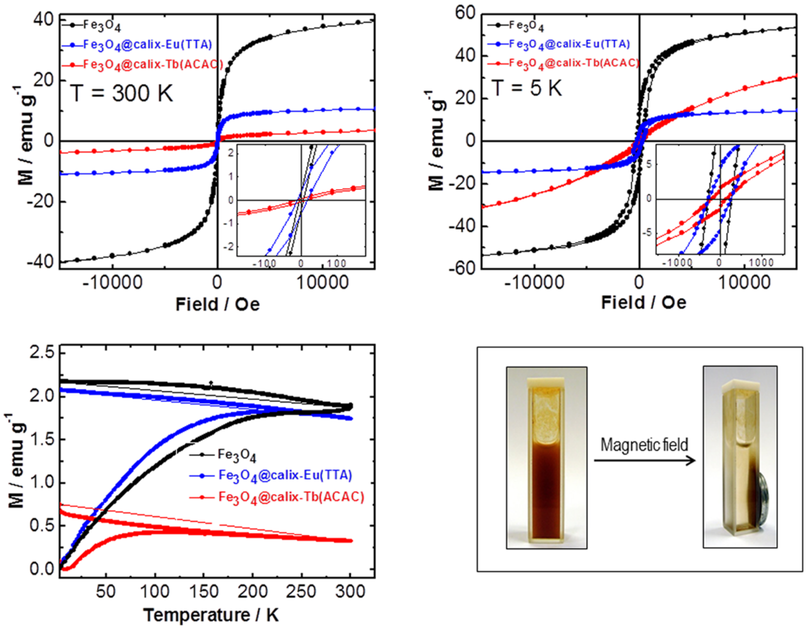

Figure 4. *M-H* curves of (clockwise from top left): Fe_3O_4, Fe_3O_4@calix-Eu(TTA), and Fe_3O_4@calix-Tb(ACAC) nanomaterials at room (300 K) and low temperature (5 K) as well as the ZFC and FC curves of Fe_3O_4, Fe_3O_4@calix-Eu(TTA) and Fe_3O_4@calix-Tb(ACAC), at 50 Oe applied field. The magnetic separation−redispersion process of Fe_3O_4@calix-Eu(TTA) nanomaterial (photo).

noncrystalline phase (possible organic) as shown in the HRTEM images. In addition, TEM images show that the nanoparticles are roughly of spherical or cubic shape, depending on the nanoparticle average size with diameters between 15 and 25 nm. This is in accordance with the SAXS analyses, where the fit was performed on the scattering data, considering a distribution of approximately spherical nanoparticles. The nanoparticles have an average diameter of ∼26 nm for both Fe_3O_4@calix-Eu(TTA) and Fe_3O_4@calix-Tb-(ACAC) nanomaterials The similar sizes inferred from the XPD patterns and TEM images suggest that the produced magnetic luminescent nanoparticles are single crystals, and this is corroborated by HRTEM images. They show that the particles are faceted single crystals with roughly spherical or cubic shape and with lattice fringes corresponding to crystallographic planes of the cubic lattice of the spinel structure, correspond to *d*-spacing such as (in nm): (i) 0.294 (220), (ii) 0.245 (311), (iii) 0.208 (400), and (iv) 0.140 (440) as shown in the SAED pattern (see Supporting Information, Figure S5 and Table S1).

3.2. Magnetic Properties. The *M-H* measurements were done at 300 and 5 K with cycling applied magnetic field between +20 and −20 kOe (1 Oe = 79.577 Am^{-1}). The results (Figure 4) include the hysteretic *M-H* curves of the Fe_3O_4, Fe_3O_4@calix-Eu(TTA), and Fe_3O_4@calix-Tb(ACAC) nanomaterials, with the saturation magnetization (M_S) values of 40, 11, and 4 emu/g, respectively. The decrease in the M_S value of the Eu^{3+} and Tb^{3+} nanomaterials when compared to the standard magnetite nanoparticles can be ascribed to (a) reduction of crystalline order as indicated by the XPD patterns (Figure 2), (b) surface effect due to the existence of smaller-sized nanoparticles, as observed in the TEM images (Figure 3), (c) presence of organic coating on the surface of magnetite nanoparticles caused by the functionalization with the calixarene and RE^{3+} β-diketonate compounds, and (d) acid-damaged magnetite nanoparticles when the calixarenes were introduced in the reaction medium. In this case, the complexes contribute to a nonmagnetic mass in the saturation magnetization calculation. Almost zero coercivity and zero remanance (less than 17 Oe and 0.3 emu g^{-1}, respectively) on the magnetization curves indicate superparamagnetic behavior at room temperature for the magnetite as well as Eu^{3+} and Tb^{3+} nanomaterials. On the other hand, all of the three nanomaterials no longer present a superparamagnetic behavior at low temperature (5 K) (Figure 4).

At 5 K, the observed coercivities are of the order of 260, 258, and 190 Oe and remanencies are 14, 4.0, and 1.5 emu g^{-1} for the Fe_3O_4, Fe_3O_4@calix-Eu(TTA), and Fe_3O_4@calix-Tb-(ACAC) nanomaterials, respectively, signature of the blocked regime. Concerning the saturation magnetization of these nanomaterials, the same trends were observed in behavior both at room and low temperatures. The only difference is that the high-field magnetization of the Fe_3O_4@calix-Tb(ACAC) nanomaterial is higher than that of the Fe_3O_4@calix-Eu(TTA) one. This fact could be attributed to the combination of the higher magnetic moment of Tb^{3+} ion (9.8 Bohr magneton) in comparison to that one of Eu^{3+} ion (3.3 Bohr magneton) with the Curie constant of respective ions. The latter one is much higher in the case of Tb^{3+} ion with the $^7F_6$ ground state and total angular momentum ($J = 6$) than in the Eu^{3+} system, which shows $^7F_0$ ground state ($J = 0$). Therefore, an abrupt increase of magnetic susceptibility was observed at low temperature (5 K) and relatively high magnetic field (higher than 300 Oe) for Fe_3O_4@calix-Tb(ACAC) nanomaterial. This result indicates that the paramagnetic contributions due to the Tb^{3+} ions cannot be neglected at low temperatures and at magnetic field higher than 300 Oe.

The ZFC/FC curves (Figure 4) of the Fe_3O_4@calix-Eu(TTA) and Fe_3O_4@calix-Tb(ACAC) nanomaterials with values of 218(2) and 110(2) K, respectively, suggest the lower blocking and irreversibility temperatures than for the standard Fe_3O_4 nanoparticles. The value obtained for the Eu^{3+} nanomaterial was found smaller or near to the standard magnetite. The behavior of the magnetization as a function of temperature (measured with an applied field of 50 Oe) was found similar for both the Eu^{3+} nanomaterial and the standard magnetite, whereas it was completely different for the Tb^{3+} system. The decrease in the blocking and irreversibility temperature of both Eu^{3+} and Tb^{3+} nanomaterials could be attributed to the existence of smaller magnetic nanoparticles. Moreover, considering SAXS measurements, there is no considerable difference in size distribution between the nanoparticles for both samples (Figure 3). The observed difference in blocking and irreversibility temperatures may also be due to an increase in the distance between the magnetic nanoparticles generated by the presence of different RE^{3+} ions. This sort of increase in the distance, caused by "external capping" of the rare earth ions, generates a reduction in the possible existence of dipolar interaction.

On the basis of this hypothesis, it could be expected that the external capping of the Tb^{3+} nanomaterial is larger than the Eu^{3+} one. This is consistent with the reduction of magnetization observed in the *M-H* and ZFC/FC data.

3.3. Photoluminescence Properties.

Fe_3O_4@calix-Gd(TTA) and Fe_3O_4@calix-Gd(ACAC) Phosphorescence. To determine the triple state (T_1) positions of the β-diketonate (TTA or ACAC) ligands on the nanoparticle surfaces, the emission spectra of the gadolinium nanomaterials were recorded with excitation at the $S_0 \rightarrow S_1$ intraligand transition. The advantage of using the Gd^{3+} ion is due to the concept that its compounds can simulate structural properties of the Eu^{3+} and Tb^{3+} complexes and also due to the first excited level ($^6P_{7/2}$) of Gd^{3+} ion located at 32 000 cm^{-1}, which is above the T_1 state of the β-diketonate ligands.[39] Therefore, the Gd^{3+} ion cannot accept energy from the lower-lying excited T_1 state of the TTA and ACAC ligands via intramolecular ligand-to-metal energy transfer. As a result, the emission spectra of the gadolinium materials show only the phosphorescence from the T_1 states, providing information about the structure of the energy levels of the β-diketonate ligands.

The emission spectra of the Fe_3O_4@calix-Gd(TTA) and Fe_3O_4@calix-Gd(ACAC) nanomaterials were recorded in the spectral range from 400 to 750 nm at 77 K under excitation at 350 and 330 nm, respectively. The T_1 state energies of the TTA and ACAC ligands in Eu^{3+} and Tb^{3+} nanomaterials were estimated as energy corresponding to the shortest emission wavelength (0−0 phonon transition), based on the phosphorescence spectra (see Supporting Information, Figure S6). They were found at 20 490 and 26 520 cm^{-1} for the TTA and ACAC ligands, respectively.

Fe_3O_4@calix-Eu(TTA) Red Phosphor. The excitation spectrum (Figure 5) of the Eu^{3+} nanomaterial was used to monitor the $^5D_0 \rightarrow {}^7F_2$ hypersensitive transition (611 nm) of the Eu^{3+} ion. The distinct broad absorption band centered at 372 nm is assigned to the TTA ligand. The absence of the narrow absorption peaks arising from the $^7F_{0,1} \rightarrow {}^5D_J$, ^5F_J, ^5H_J, ^5G_J, and ^5L_J transitions of Eu^{3+} is consistent with the concept that the luminescence sensitization through intramolecular energy transfer from the TTA ligands to Eu^{3+} ion is very efficient.

The emission spectrum of the Fe_3O_4@calix-Eu(TTA) nanomaterial (Figure 5) was recorded at 77 K and room temperature (see Supporting Information, Figure S7) in the range of 400−750 nm, under excitation to the intraligand $S_0 \rightarrow S_1$ transition of the TTA ligand. This spectrum exhibits groups of narrow emission bands assigned to the $^5D_0 \rightarrow {}^7F_J$ transitions (where J = 0−4), dominated by the $^5D_0 \rightarrow {}^7F_2$ hypersensitive one. The absence of the broad emission band centered at 525 nm, from the triplet state (T_1) of the TTA ligand,[39] is also consistent with an efficient ligand-to-metal intramolecular energy transfer.

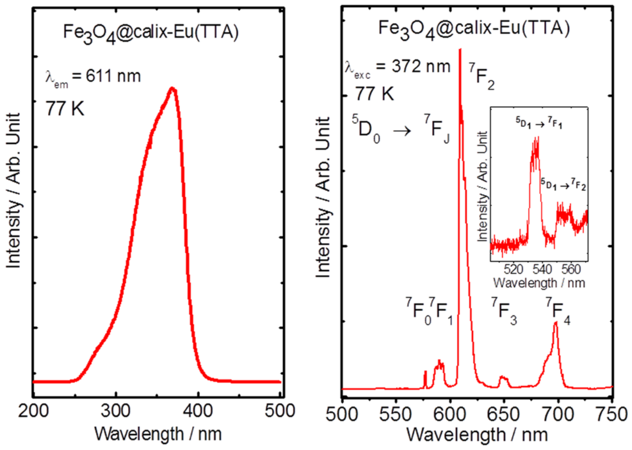

Figure 5. Luminescence spectra of the Fe_3O_4@calix-Eu(TTA) nanophosphor recorded at low temperature (77 K): excitation (left) spectrum monitoring emission at 611 nm assigned to the $^5D_0 \rightarrow {}^7F_2$ transition and emission (right) spectrum under excitation at 372 nm, which corresponds to the $S_0 \rightarrow S_1$ transition of the organic ligands.

The experimental intensity parameters Ω_λ (λ = 2 and 4) were determined for the Fe_3O_4@calix-Eu(TTA) system from the emission data recorded at room temperature. The Ω_λ, also known as the Judd−Ofelt parameters, are determined by the intensities of the $^5D_0 \rightarrow {}^7F_J$ transitions (J = 2 and 4) of the Eu^{3+} ion, and the forced electric dipole and dynamic coupling mechanisms are considered simultaneously. Under normal excitation conditions, the emission intensities (I) of the bands may be given by the expression[40]

$$I_{0\rightarrow J} = \hbar\omega_{0\rightarrow J} A_{0\rightarrow J} N_0 \tag{1}$$

where $\hbar\omega_0$ is the energy of the transition (in cm^{-1}), N_0 is the population of the emitting $^5D_0$ level, and $A_{0\rightarrow J}$ are the coefficients of spontaneous emission. For the experimental determination of the $A_{0\rightarrow J}$ emission coefficients from the emission spectra, the special character of the magnetic dipole-allowed $^5D_0 \rightarrow {}^7F_1$ transition was exploited. This 4f−4f transition is formally insensitive to the chemical environment around the Eu^{3+} ion and, consequently, can be used as a reference.[40] The values of Ω_λ are obtained from eq 2 as follows:

$$A_{0\rightarrow J} = \frac{4e^2\omega^3}{3\hbar c^3}\frac{1}{2J+1}\chi \sum_{\lambda=2,4,6} \Omega_\lambda \langle {}^5D_0 \| U^{(\lambda)} \| {}^7F_J \rangle^2 \tag{2}$$

where $\chi = (n_0(n_0^2 + 2)^2)/(9)$ is the Lorentz local field correction, and n_0 is the refractive index of the medium (n_0 assumed to be equal to 1.5). The squared reduced matrix elements $\langle {}^5D_0 \| U^{(\lambda)} \| {}^7F_J \rangle^2$ have values of 0.0032 and 0.0023 for J = 2 and 4, respectively. The coefficients of spontaneous emission ($A_{0\rightarrow J}$) are then obtained from eq 3:

$$A_{0\rightarrow J} = \left(\frac{\sigma_{0\rightarrow 1}}{S_{0\rightarrow 1}}\right)\left(\frac{S_{0\rightarrow J}}{\sigma_{0\rightarrow J}}\right) A_{0\rightarrow 1} \tag{3}$$

where the $S_{0\rightarrow J}$ factors correspond to the integrated area under the curve related to the $^5D_0 \rightarrow {}^7F_J$ transition and $\sigma_{0\rightarrow J}$ are the energy barycenters of the transitions. The emission quantum efficiency (η) of the emitting $^5D_0$ level is determined according to eq 4:[39]

Table 1. Experimental Intensity Parameters (Ω_λ), Lifetimes τ, Emission Coefficient Rates A_{rad} and A_{nrad} as well as the Emission Quantum Efficiencies η for the Fe_3O_4@calix-Eu(TTA) Nanomaterial

materials	Ω_2 (10^{-20} cm^{-2})	Ω_4 (10^{-20} cm^{-2})	A_{rad} (s^{-1})	A_{nrad} (s^{-1})	A_{tot} (s^{-1})	τ (ms)	η (%)
Fe_3O_4@calix-Eu(TTA)	15	9	633	3714	4348	0.23	14
$[Eu(TTA)_3(H_2O)_2]^a$	33	5	1110	2730	3846	0.26	29

[a] Reference 40.

$$\eta = \frac{A_{rad}}{A_{rad} + A_{nrad}} \tag{4}$$

The total decay rate corresponds to $A_{tot} = (1/\tau) = A_{rad} + A_{nrad}$, where A_{rad} $(= \sum_J A_{0\to J})$ and A_{nrad} are the total radiative and nonradiative rates, respectively.

On the basis of theoretical considerations, the intensity Ω_2 parameter is mostly influenced by small angular changes in the local coordination geometry.[46,47] This effect together with changes in the polarizabilities (α) of ligating atoms has been used to rationalize the hypersensitive character of certain 4f intraconfigurational transitions to changes in the chemical environment. The fact that the Ω_2 and Ω_4 parameters of Fe_3O_4@calix-Eu(TTA) nanophosphor (Table 1) have different values to the $[Eu(TTA)_3(H_2O)_2]$ complex is an indication of different chemical environment around the Eu^{3+} ion. In addition, the low Ω_2 value for the Eu^{3+} nanomaterial when compared to the corresponding complex indicates hypersensitivity character of the $^5D_0 \to {}^7F_2$ transition of the Eu^{3+} ion.[46]

The value of the emission quantum efficiency of $^5D_0$ level for the Fe_3O_4@calix-Eu(TTA) phosphor (η = 14%) is lower than that for the $[Eu(TTA)_3(H_2O)_2]$ complex (η = 29%) (Table 1). This result indicates that multiphonon relaxation due to OH groups in calixarene, magnetite, and the presence of water molecules in the coordination sphere is more operative in the nanomaterial, leading to a higher nonradiative decay rate (A_{nrad} = 3714 s^{-1}). Nevertheless, this phosphor yields considerable luminescence intensity, indicating that the photoluminescent magnetic nanomaterial may be a good candidate for preparation of the emitting layer of magnetic and red light-converting molecular devices (MLCMDs).

Fe_3O_4@calix-Tb(ACAC) Green Phosphor. The excitation spectrum of the Tb^{3+} nanomaterial was recorded in the range of 200−400 nm, monitoring emission at 545 nm assigned to the $^5D_4 \to {}^7F_5$ transition of the Tb^{3+} ion. The spectrum (Figure 6) shows a broad absorption band centered at 323 nm and assigned to the $S_0 \to S_1$ transition of the ACAC ligand. No narrow absorption lines due to transitions within the $4f^8$ electron configuration of the Tb^{3+} ion can be observed. As a conclusion, it is suggested that the Fe_3O_4@calix-Tb(ACAC) nanomaterials can serve as green phosphors due to efficient intramolecular energy transfer from the ACAC ligands to the terbium ion.

The emission spectrum of the Fe_3O_4@calix-Tb(ACAC) nanomaterial was recorded in the range of 450 to 700 nm at liquid nitrogen and room temperatures, under excitation at ~323 nm corresponding to the $S_0 \to S_1$ transition of the ACAC ligand (Figure 6 and Supporting Information, Figure S8). The groups of narrow emission lines were assigned to the $^5D_4 \to {}^7F_J$ transitions (J = 6−0) of the Tb^{3+} ion. The emission data indicate the $^5D_4 \to {}^7F_5$ transition at ~545 nm as the most intense one that results in the green emission color. Similar to the Fe_3O_4@calix-Eu(TTA) phosphor, the broad phosphorescence band of the ligand was not observed, indicating a very operative intramolecular energy transfer from the ACAC ligand to the Tb^{3+} ion.

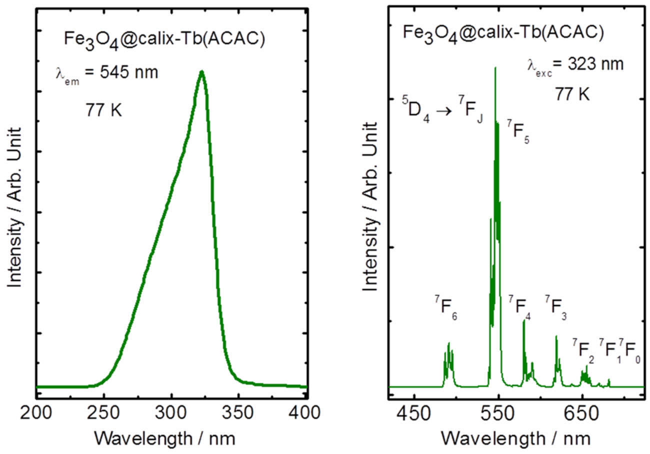

Figure 6. Luminescence spectra of the Fe_3O_4@calix-Tb(ACAC) recorded at low temperature (77 K). Excitation (left) spectrum, monitoring emission at 545 nm assigned to the $^5D_4 \to {}^7F_5$ transition. Emission (right) spectrum under excitation at 323 nm, which corresponds to the $S_0 \to S_1$ transition of the organic ligands.

Intramolecular Energy Transfer. From the photoluminescence data, the nonradiative energy transfer pathways from the β-diketonate ligands to Eu^{3+} and Tb^{3+} ions in both phosphors may be described using a theoretical model proposed earlier.[40] Recently, it has been shown[48] that the main luminescence sensitization path in the $[Eu(TTA)_3(H_2O)_2]$ complex occurs through the energy transfer from the first T_1 excited state of the TTA ligand to the $^5D_1$ excited level of the Eu^{3+} ion (Figure 7).

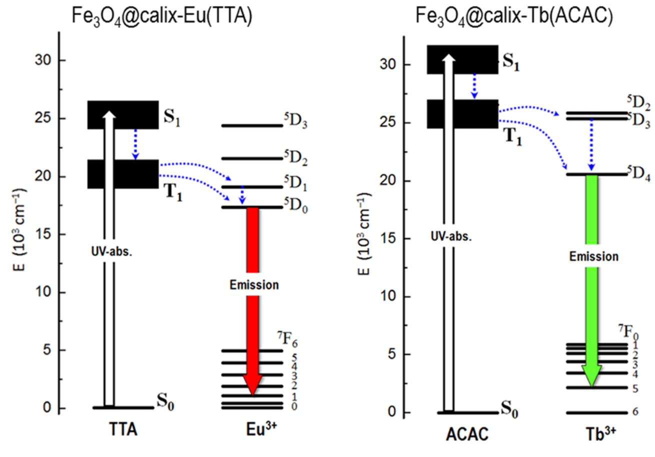

Figure 7. Partial energy level diagrams of the Fe_3O_4@calix-Eu(TTA) (left) and Fe_3O_4@calix-Tb(ACAC) (right) nanophosphors. The dashed arrows represent nonradiative decays, and the red and green color arrows correspond to the radiative decays of the Eu^{3+} and Tb^{3+} ions, respectively. The former are most probable intramolecular energy transfer processes from the β-diketonate to rare earth ion.

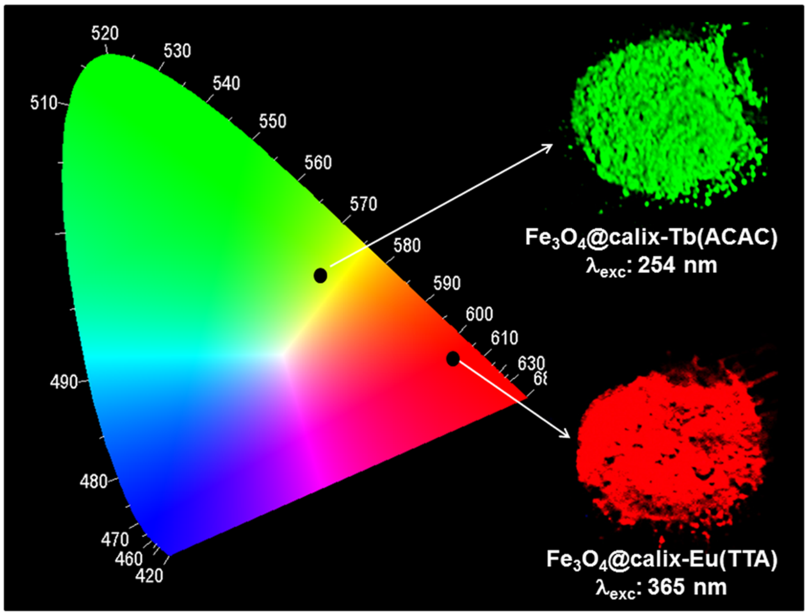

Figure 8. CIE chromaticity diagram showing the (*x*, *y*) emission color coordinates for Fe_3O_4@calix-Eu(TTA) and Fe_3O_4@calix-Tb(ACAC) nanophosphors irradiated at different wavelengths. Photographs of nanomaterials (inset) taken with a digital camera displaying the green and red emissions under UV irradiation lamp at 254 and 365 nm, respectively.

Among the β-diketonate ligands, ACAC has an appropriate triplet state energy (26 520 cm^{-1}) for intramolecular energy transfer to the emitting $^5D_4$ level of the Tb^{3+} ion (~20 400 cm^{-1}). Taking into account that the emitting $^5D_4$ level of the Tb^{3+} ion is higher than the $^5D_0$ excited level of Eu^{3+} ion, the ACAC ligand is by far a better luminescence sensitizer for the Tb^{3+} ion than the TTA ligand (Figure 7). For the Fe_3O_4@calix-Tb(ACAC) phosphor, the energy gap $\Delta E(T_1{-}^5D_4)$ is ~6000 cm^{-1}, which avoids the possibility of an energy back transfer from the Tb^{3+} ion.

The Eu^{3+} phosphor shows (*x*, *y*) color coordinates (x = 0.6155 and y = 0.3330) in the red region of the CIE chromaticity diagram (CIE = Commission Internationale de l'Eclairage) mainly due to the high intensity of the hypersensitive $^5D_0 \rightarrow {}^7F_2$ transitions at 611 nm of the Eu^{3+} ion (Figure 8). On the other hand, the Tb^{3+} nanomaterial displays green-yellowish emission color with (x = 0.4119 and y = 0.4691) color coordinates due to the $^5D_4 \rightarrow {}^7F_{6-0}$ transitions of the Tb^{3+} ion. A gradual shift in the (*x*, *y*) color coordinates is observed from the green to the yellow spectral region due to the increased contribution from the emission to the $^7F_{4-0}$ energy levels. These superparamagnetic nanomaterials also can act as efficient phosphors for light-conversion molecular devices (LCMDs), displaying red and green emission colors arising from the Eu^{3+} and Tb^{3+} ions (see Supporting Information, Movie S1).

4. CONCLUSIONS

Bifunctional optical-magnetic nanomaterials of the Eu^{3+} and Tb^{3+} ions were successfully prepared by a new method, involving one-pot synthesis. All of the nanomaterials exhibit superparamagnetic behavior at room temperature. In addition, the photoluminescence data suggest that the TTA and ACAC ligands act as efficient sensitizers for the red (Eu^{3+}) and green (Tb^{3+}) emission in the nanomaterials, though their emission efficiencies are lower than in the complexes. As a result, they are good candidates for the preparation of emitting layers in magnetic light-converting molecular devices (MLCMDs). Moreover, they may be applied as contrast agents in magnetic resonance imaging and magnetic luminescent biomarkers, a project that is being launched in the group.

■ ASSOCIATED CONTENT

Ⓢ Supporting Information

Synthesis (procedure and illustration) of the calixarene ligand, ^1H, ^{13}C, and DEPT-135 NMR spectra of calixarene ligand, FTIR absorption spectra of the calixarene ligand and nanomaterials, SAED patterns, emission spectra of Gd^{3+} nanomaterials, tabulated crystallographic data, and a movie showing USP being used to write. This material is available free of charge via the Internet at http://pubs.acs.org.

■ AUTHOR INFORMATION

Corresponding Author

*E-mail: hefbrito@iq.usp.br. Phone: +55 11 3091 3847. Fax: +55 11 3815 5579.

Notes

The authors declare no competing financial interest.

■ ACKNOWLEDGMENTS

The authors are grateful for financial support from the Conselho Nacional de Desenvolvimento Científico e Tecnológico (CNPq, Brazil), Fundação de Amparo à Pesquisa do Estado de São Paulo (FAPESP, Brazil), Instituto Nacional de Ciência e Tecnologia de Nanotecnologia para Marcadores Integrados (inct-INAMI, Brazil), Coordenação de Aperfeiçoamento de Pessoal de Nível Superior (CAPES, Brazil), CNPEM-LNLS synchrotron, Campinas-SP, Brazil under Proposal Nos. SAXS1−14355 (7959), CNPEM-LNNano, Campinas-SP, Brazil under Proposal Nos. TEM-MSC 14828 (7959) and Academy of Finland (Project No. 137333/2010).

■ REFERENCES

(1) Vollath, D. *Adv. Mater.* **2010**, *22*, 4410−4415.

(2) Lin, Y.-S.; Wu, S.-H.; Hung, Y.; Chou, Y.-H.; Chang, C.; Lin, M.-L.; Tsai, C.-P.; Mou, C. Y. *Chem. Mater.* **2006**, *18*, 5170−5172.

(3) Huh, Y.-M.; Jun, Y.-W.; Song, H.-T.; Kim, S.; Choi, J.-S.; Lee, J.-H.; Yoon, S.; Kim, K. S.; Shin, J.-S.; Suh, J.-S.; Cheon, J. *J. Am. Chem. Soc.* **2005**, *127*, 12387−12391.

(4) Giri, S.; Trewyn, B. G.; Stellmarker, M. P.; V. Lin, S.-Y. *Angew. Chem., Int. Ed.* **2005**, *44*, 5038−5044.

(5) Kim, J.; Lee, J. E.; Lee, J.; Jang, Y.; Kim, S.-W.; An, K.; Yu, J. H.; Hyeon, T. *Angew. Chem., Int. Ed.* **2006**, *45*, 4789−4793.

(6) Yu, H.; Chen, M.; Rice, P. M.; Wang, S. X.; White, R. L.; Sun, S. *Nano Lett.* **2005**, *5*, 379−382.

(7) Shi, W.; Zeng, H.; Sahoo, Y.; Ohulchanskyy, T. Y.; Ding, Y.; Wang, Z. L.; Swihart, M.; Prasad, P. N. *Nano Lett.* **2006**, *6*, 875−881.

(8) Salgueirino-Maceira, V.; Correa-Duarte, M. A.; Spasova, M.; Liz-Marzan, L. M.; Farle, M. *Adv. Funct. Mater.* **2006**, *16*, 509−514.

(9) Yi, D. K.; Selvan, S. T.; Lee, S. S.; Papaefthymiou, G. C.; Kundaliya, D.; Ying, J. Y. *J. Am. Chem. Soc.* **2005**, *127*, 4990−4991.

(10) Yu, S.-Y.; Zhang, H.-J.; Yu, J.-B.; Wang, C.; Sun, L.-N.; Shi, W.-D. *Langmuir* **2007**, *23*, 7836−7840.

(11) Kell, A. J.; Barnes, M. L.; Jakubek, Z. J.; Simard, B. *J. Phys. Chem. C* **2011**, *115*, 18412−18421.

(12) Son, A.; Dhirapong, A.; Dosev, D. K.; Kennedy, I. M.; Weiss, R. H.; Hristova, K. R. *Anal. Bioanal. Chem.* **2008**, *390*, 1829−1835.

(13) Chen, H.; Colvin, D. C.; Qi, B.; Moore, T.; He, J.; Mefford, O. T.; Alexis, F.; Gore, J. C.; Anker, J. N. *J. Mater. Chem.* **2012**, *22*, 12802−12809.

(14) Griffete, N.; Herbst, F.; Pinson, J.; Ammar, S.; Mangeney, C. *J. Am. Chem. Soc.* **2011**, *133*, 1646−1649.

(15) Kirschvink, J. L.; Kobayashi-Kirschvink, A.; Woodford, B. J. *Proc. Natl. Acad. Sci. U.S.A.* **1992**, *89*, 7683−7687.

(16) Herndon, J. M.; Rowe, M. W.; Larson, E. E.; Watson, D. E. *Nature* **1975**, *253*, 516−517.

(17) Bazylinski, D. A.; Frankel, R. B.; Jannasch, H. W. *Nature* **1988**, *334*, 518−519.

(18) Mandernack, K. W.; Bazylinski, D. A.; Shanks lll, W. C.; Bullen, T. D. *Science* **1999**, *285*, 1892−1896.

(19) Lovley, D. R.; Stolz, J. F.; Nord, G. L., Jr.; Phillips, E. J. P. *Nature* **1987**, *330*, 252−254.

(20) Diebel, C. E.; Proksch, R.; Green, C. R.; Neilson, P.; Walker, M. M. *Nature* **2000**, *406*, 299−302.

(21) Hsu, C.-Y.; Li, C.-W. *Science* **1994**, *265*, 95−97.

(22) Tamaura, Y.; Tabata, M. *Nature* **1990**, *346*, 255−256.

(23) Tadmor, R.; Rosensweig, R. E.; Frey, J.; Klein, J. *Langmuir* **2000**, *16*, 9117−9120.

(24) Rosensweig, R. E.; Kaiser, R.; Miskolczy, G. *J. Colloid Interface Sci.* **1969**, *29*, 680−686.

(25) Rockenberger, J.; Scher, E. C.; Alivisatos, A. P. *J. Am. Chem. Soc.* **1999**, *121*, 11595−11596.

(26) Yee, C.; Kataby, G.; Ulman, A.; Prozorov, T.; White, H.; King, A.; Rafailovich, M.; Sokolov, J.; Gedanken, A. *Langmuir* **1999**, *15*, 7111−7115.

(27) Dupont, D.; Brullot, W.; Bloemen, M.; Verbiest, T.; Binnemans, K. *ACS Appl. Mater. Interfaces* **2014**, *6*, 4980−4988.

(28) Chin, S. F.; Makha, M.; Raston, C. L.; Saunders, M. *Chem. Commun.* **2007**, 1948−1950.

(29) Özkinal, S.; Kocaokutgen, H. *J. Mol. Struct.* **2013**, *1031*, 70−78.

(30) Creavena, B. S.; Donlona, D. F.; McGinley, J. *Coord. Chem. Rev.* **2009**, *253*, 893−962.

(31) Oueslati, I.; Sá Ferreira, R. A.; Carlos, L. D.; Baleizão, C.; Berberan Santos, M. N.; Castro, B.; Vicens, J.; Pischel, U. *Inorg. Chem.* **2006**, *45*, 2652−2660.

(32) Liu, Z.; Jiang, L.; Liang, Z.; Gao, Y. *Tetrahedron Lett.* **2005**, *46*, 885−887.

(33) Steemers, F. J.; Verboom, W.; Reinhoudt, D. N.; van der Tol, E. B.; Verhoeven, J. W. *J. Am. Chem. Soc.* **1995**, *117*, 9408−9414.

(34) Steemers, F. J.; Meuris, H. G.; Verboom, W.; Reinhoudt, D. N. *J. Org. Chem.* **1997**, *62*, 4229−4235.

(35) Bünzli, J.-C. G.; Eliseeva, S. V. *Chem. Sci.* **2013**, *4*, 1939−1949.

(36) Bünzli, J.-C. G. *Chem. Rev.* **2010**, *110*, 2729−2755.

(37) Rodrigues, L. C. V.; Hölsä, J.; Lastusaari, M.; Felinto, M. C. F. C.; Brito, H. F. *J. Mater. Chem. C* **2014**, *2*, 1612−1618.

(38) Kai, J.; Felinto, M. C. F. C.; Nunes, L. A. O.; Malta, O. L.; Brito, H. F. *J. Mater. Chem.* **2011**, *21*, 3796−3802.

(39) Carlos, L. D.; Messaddeq, Y.; Brito, H. F.; Sá Ferreira, R. A.; Bermudez, V. Z.; Ribeiro, S. J. L. *Adv. Mater.* **2000**, *12*, 594−598.

(40) de Sá, G. F.; Malta, O. L.; Donegá, C. M.; Simas, A. M.; Longo, R. L.; Santa Cruz, P. A.; da Silva, E. F., Jr. *Coord. Chem. Rev.* **2000**, *196*, 165−195.

(41) Gutsche, C. D.; Lin, L.-G. *Tetrahedron* **1986**, *42*, 1633−1640.

(42) Gutsche, C. D.; Nam, K. C. *J. Am. Chem. Soc.* **1988**, *110*, 6153−6162.

(43) Sharma, S. K.; Kanamathareddy, S.; Gutsche, C. D. *Synthesis* **1997**, *11*, 1268−1272.

(44) Atwood, J. L.; Hamada, F.; Robinson, K. D.; Orr, G. W.; Vincent, R. L. *Nature* **1991**, *349*, 683−684.

(45) Fang, J.; Saunders, M.; Guo, Y.; Lu, G.; Raston, C. L.; Iyer, K. S. *Chem. Commun.* **2010**, *46*, 3074−3076.

(46) Sá Ferreira, R. A.; Nobrea, S. S.; Granadeiro, C. M.; Nogueira, H. I. S.; Carlos, L. D.; Malta, O. L. *J. Lumin.* **2006**, *121*, 561−567.

(47) Borges, A. S.; Dutra, J. D. L.; Freire, R. O.; Moura, R. T., Jr.; Da Silva, J. G.; Malta, O. L.; Araujo, M. H.; Brito, H. F. *Inorg. Chem.* **2012**, *51*, 12867−12878.

(48) Faustino, W. M.; Nunes, L. A.; Terra, I. A. A.; Felinto, M. C. F. C.; Brito, H. F.; Malta, O. L. *J. Lumin.* **2013**, *137*, 269−273.